Journal of Alloys and Compounds 929 (2022) 167065

Contents lists available at ScienceDirect

Journal of Alloys and Compounds

journal homepage: www.elsevier.com/locate/jalcom

Superparamagnetic and light-emitting bifunctional nanocomposites of iron oxide and erbium or thulium doped yttrium orthovanadate

María Rapp[a,*], Yaiza Lozano[a], Miguel Fernández-Ramos[a,b], Josefa Isasi[a], Mauricio Alcolea Palafox[b,*]

[a] Departamento de Química Inorgánica, Facultad de Ciencias Químicas, Universidad Complutense de Madrid, Ciudad Universitaria s/n, 28040 Madrid, Spain
[b] Departamento de Química-Física, Facultad de Ciencias Químicas, Universidad Complutense de Madrid, Ciudad Universitaria s/n, 28040 Madrid, Spain

ARTICLE INFO

Article history:
Received 22 June 2022
Received in revised form 31 August 2022
Accepted 1 September 2022
Available online 5 September 2022

Keywords:
Rare earth doped orthovanadates
Lanthanide emission
Superparamagnetic nanoparticles
Bifunctional materials
Silica-covered nanopowders

ABSTRACT

Advances in biomedical research have increased interest in obtaining and studying new bifunctional materials for use in theragnostic. Here we describe in detail the preparation of new magnetic-fluorescent bifunctional $(Y_{0.9}Ln_{0.1}VO_4/Fe_3O_4)@SiO_2$ and $[(Y_{0.9}Ln_{0.1}VO_4\ @SiO_2)/Fe_3O_4)@SiO_2]$ nanocomposites with Ln = Er or Tm. In addition, their magnetic and optical properties were carefully analyzed. The influence of Fe_3O_4 content and the silica shell thickness on the fluorescent emission in the VIS-NIR region of $Y_{0.9}Ln_{0.1}VO_4$ cores was evaluated as well as their use as display systems with the possibility of directing them by means of external magnetic fields. Samples were prepared using wet chemistry methods involving low temperatures and short reaction times. $Y_{0.9}Ln_{0.1}VO_4$ samples that are not easily oxidizable were prepared by a hydrothermal method, while Fe_3O_4 sample was synthesized by a coprecipitation process in which the mixture of precursors was treated at very low temperature to avoid oxidation. The powder amalgamation of both $Y_{0.9}Ln_{0.1}VO_4$ and Fe_3O_4 samples was possible due to the silica polymeric network synthetized by a modified Stöber method. The purity of all samples was ensured by XRD and FTIR techniques. Diffraction profiles of $Y_{0.9}Ln_{0.1}VO_4$ samples show diffraction maxima that can be indexed to a tetragonal symmetry of space group $I4_1/amd$, compatible with the zircon structure-type of YVO_4 host. All reflections present in the diffraction profile of Fe_3O_4 sample can be indexed to a cubic symmetry of space group $Fd\bar{3}m$, characteristic of an inverse spinel structure-type. The amorphous silica incorporation on the samples was also evaluated by TEM images. Studies of the magnetic behavior and luminescent emission intensity of the investigated samples showed their dependence on both, the silica coating thickness, and the contact or not between the luminescent samples and the magnetic powder.

1. Introduction

Bifunctional materials that combine magnetic and optical properties in a single entity are attracting growing interest due to their potential application in the biomedicine field, either as drug delivery systems, fluorescent thermometers in photothermal therapy or in bioimaging or hyperthermia applications [1–6]. For these purposes, materials based on rare earth-doped luminescent nanoparticles [4,6–8] and/or superparamagnetic Fe_3O_4 nanoparticles are currently being synthesized and studied [6,9–11].

Among all the samples of materials used as phosphors, those based on the emission of lanthanide ions stand out for their greater stability, biocompatibility, and lower toxicity compared to others that are also used, such as quantum dots (QDs) or organic dyes [1]. Furthermore, the inorganic host lattice containing the lanthanide ions plays a key role and must be considered when looking for new applications, selecting different compositions in the samples to be synthesized.

The β-$NaYF_4$ compound is one of the most widely used inorganic host lattices [4,5]. Its low phonon energy (~350 cm^{-1}) provides a low energy loss due to non-radiative transitions and consequently, the light emission is enhanced [5]. Samples of this fluoride and its derivatives are still under investigation [12–15]. However, due to its high hygroscopicity, its use in biomedicine is limited, thus requiring much more stable compounds such as oxides [3,16,17]. Among them, we are studying yttrium orthovanadate (YVO_4) doped with lanthanide ions. This host matrix has good mechanical and thermal properties [1,4,18] and, despite its high phonon energy (700–900 cm^{-1}), light emission from lanthanide ions (Ln^{3+}) is very efficient [4,19,20]. The VO_4^{3-} groups display strong UV light

* Corresponding authors.
E-mail addresses: mrapp@ucm.es (M. Rapp), alcolea@ucm.es (M.A. Palafox).

https://doi.org/10.1016/j.jallcom.2022.167065

absorption, but they do not show light emission because the absorbed energy is dissipated non-radiatively through quenching sites [4,21]. However, lanthanide ions show light emission due to 4f–4f and 4f-5d electronic transitions, so the host lattice can efficiently absorb radiation and then non-radiatively transfer it to Ln^{3+} ions [22,23].

For a long time, research has also been carried out to obtain magnetic nanoparticles of magnetite (Fe_3O_4) that are currently of great interest due to their large potential for use in many technological applications. Nanoparticles of this composition, smaller than 15 nm, offer unique advantages over other materials, such as that they can be synthesized by low-cost methods, they are physically and chemically stable, biocompatible, and non-toxic [9,24]. They also have strong magnetic saturation and superparamagnetism at room temperature, which means that these nanoparticles can be temporarily magnetized in presence of an external magnetic field and this magnetization disappears when the field is removed [9,16,25].

The nanometric size of magnetic and fluorescent samples is a critical parameter that will affect their use. The same feature appears with magnetic-fluorescent bifunctional samples of Fe_3O_4 and lanthanide ions-doped orthovanadates, especially when it comes to use in biomedicine. Their toxicity and efficacy will depend on the particle size, as well as the fluorescence emission intensity of lanthanide-doped materials, which varies with crystallinity and particle size [26,27]. Likewise, the magnetic properties will be affected, being able to find superparamagnetic behaviors below 20 nm [9,24]. These particle sizes can be controlled using different synthesis routes and methods, as well as by varying reaction parameters such as temperature, time, concentration, or pH. Among all methods used to obtain nanoparticles, the wet chemistry methods that involve low temperatures and short reaction times highlight for their mild reaction conditions. Some of these methods are hydrothermal [4,28], sol-gel [4], coprecipitation [9] or microemulsion [23]. The use of one method or another depends on whether the samples to be obtained are easily oxidizable, something that often happens when iron oxide samples are prepared. However, this is not the case with orthovanadate samples.

One of the problems associated with obtaining nanoparticles using these methods is the formation of a high density of defects on the particles surface, which negatively affects their properties (light emission and magnetic response). Once generated, these defects are often reduced by preparing core shell structures on these samples with different coatings [29]. Silica is one of the most widely used materials for encapsulation of nanoparticle samples due to its biocompatibility and stability in biological media, and it is also transparent to visible and NIR radiation [1,3,4].

In a recent paper, we have studied magnetic-fluorescent bifunctional samples of neodymium and terbium orthovanadates finding promising results that indicate their possible use in the biomedicine field. Following our research, in the present manuscript is described a complementary study of magnetic-fluorescent bifunctional $(Y_{0.9}Ln_{0.1}VO_4/Fe_3O_4)@SiO_2$ and $[(Y_{0.9}Ln_{0.1}VO_4@SiO_2)/Fe_3O_4)@SiO_2]$ samples with Ln = Er or Tm. In this case, $Y_{0.9}Er_{0.1}VO_4$ and $Y_{0.9}Tm_{0.1}VO_4$ samples were prepared by the hydrothermal method, while Fe_3O_4 sample was prepared by the coprecipitation method.

The effect of fluorescence quenching by both the magnetite sample and the silica coating thickness has been studied on the synthesized bifunctional samples.

2. Experimental

2.1. Preparation of $Y_{0.9}Ln_{0.1}VO_4$ samples by hydrothermal synthesis

$Y_{0.9}Ln_{0.1}VO_4$ samples with Ln = Er^{3+}or Tm^{3+} were prepared by hydrothermal synthesis and at basic pH. Yttrium, erbium and thulium nitrates $Y(NO_3)_3{\cdot}6\ H_2O$ (99.8%, Strem Chemicals), $Er(NO_3)_3{\cdot}5\ H_2O$ (99.9%, Strem Chemicals), $Tm(NO_3)_3{\cdot}5\ H_2O$ (99.9%, Strem Chemicals), as well as ammonium vanadate, NH_4VO_3, (≥ 99%, Sigma Aldrich) were used as starting precursors. Urea, $(NH_2)_2CO_2$, (Aldrich, 99.8%) was also employed as fuel agent and NH_3 (25%, Sigma Aldrich) was used to adjust the pH of the reaction medium.

For the preparation of $Y_{0.9}Er_{0.1}VO_4$ and $Y_{0.9}Tm_{0.1}VO_4$ samples, 0.25 g of NH_4VO_3 and stoichiometric amounts of the respective nitrates [$Y(NO_3)_3{\cdot}6\ H_2O$, $Er(NO_3)_3{\cdot}5\ H_2O$ or $Tm(NO_3)_3{\cdot}5\ H_2O$], calculated taking into account the reaction {1}, were placed in two beakers and dissolved in 50 mL of deionized water.

$$0.9\ Y(NO_3)_3.6\,H_2O + 0.1Ln(NO_3)_3{\cdot}\ 5\,H_2O + NH_4VO_3 + CO(NH_2)_2 \rightarrow$$

$$Y_{0.9}Er_{0.1}VO_4 + 3\ NH_3 + CO_2 + 3\ NO_2 + 5.4\,H_2O + 1.5\,O_2 \quad (1)$$

These solutions were heated at 100 °C under stirring for 30 min. Urea was added in a 1:1 ratio with respect to the ammonium vanadate precursor. This reagent is a fuel that also acts as a good dispersing agent, allowing the formation of a stable suspension and avoiding the agglomeration of the nanoparticles [28].

Two hours later, NH_3 (25%, Sigma Aldrich) was added to adjust the pH value to 9, and the two solutions were heated for one hour under stirring. Our previous studies indicated that this reaction medium favors the obtaining of slightly larger nanoparticles that emit with greater intensity [30,31]. These solutions were heated at 200 °C for 1 h to remove the solvent, and the resulting powders were aged for 3 days. After this time, they were re-dissolved in deionized water and placed in Teflon-lined stainless-steel autoclaves, where they were heated at 220 °C for 6 h. The obtained precipitates were dried in a stove until obtaining powders. Finally, these powders of yellow color were treated at 550 °C for 6 h. Samples obtained were named as $Y_{0.9}Er_{0.1}VO_4$ and $Y_{0.9}Tm_{0.1}VO_4$.

2.2. Synthesis of Fe_3O_4 sample by coprecipitation

0.5 g of $FeCl_3{\cdot}6\ H_2O$ (Strem Chemicals, 97%) and 0.1850 g of $FeCl_2{\cdot}4\ H_2O$ (Sigma Aldrich, 99%) were placed in a beaker and dissolved in 100 mL of deionized water. The resulting mixture was transferred into a three-neck glass flask connected to a thermostatic bath and, under mechanical stirring (200 rpm), heated at 75 °C under Ar atmosphere to avoid the oxidation of iron oxide. 30 min later, a solution of NaOH (98–100% PanReac) in water was prepared with the addition of 3 mL of NH_3 (32%). This solution was added to a the-neck glass flask, reaching a pH of 12. A color change from orange to black was immediately observed due to iron hydroxides precipitation [32].

Half hour later, 2 mL of oleic acid that acted as a dispersing agent were added [5] and the reaction was maintained for another 30 min. The iron oxide precipitate was separated by magnetic decantation and washed with acetone to remove traces of ammonia and oleic acid. The resulting black powder was dried at 75 °C for 12 h.

2.3. Preparation of silica coated samples

All samples were prepared by a modified Stöber method [1,3,4]. For the preparation of silica coated $Y_{0.9}Ln_{0.1}VO_4@SiO_2$ samples with Ln = Er or Tm, 0.1 g of the corresponding orthovanadate sample were dispersed by adding a 3:10 ratio of EtOH:H_2O mixture in a two-necked glass flask placed in an ultrasonic bath at 30°C. In this reaction medium, ethanol provides the necessary OH^- groups to facilitate the adhesion of the polymeric network ···O-Si-O-Si-O··· in the dispersed particles of the considered sample. Later, 10 mL of NH_3 were slowly added through another neck of the flask, being under stirring and heating at 75°C. Once the solution was homogenized,

2 mL of TEOS (100%, VRW Chemicals) were added dropwise for 3 h. The resulting mixture was centrifuged to separate the precipitate, washed with a 1:1 EtOH:H_2O water solution and dried at 75°C for 12 h. The obtained samples were called as $Y_{0.9}Er_{0.1}VO_4$@SiO_2 and $Y_{0.9}Tm_{0.1}VO_4$@SiO_2.

A similar procedure was used to obtain Fe_3O_4@SiO_2 sample, but in this case using a three-necked reaction flask, where the reaction was also carried out by heating to 75 °C, under mechanical stirring and in an Ar atmosphere.

For the preparation of the nanocomposites resulting from the mixture of $Y_{0.9}Er_{0.1}VO_4$, $Y_{0.9}Tm_{0.1}VO_4$ and Fe_3O_4 samples, 0.05 g of each of the samples was mixed in an agate mortar to obtain homogeneous powder samples. Later, these powders were dispersed by adding a 3:10 ratio of EtOH:H_2O mixture and 10 mL of NH_3 (30%) in a two-necked glass flask placed in an ultrasonic bath at 30°C for 10 min. The resulting mixtures were transferred to three-necked glass flasks that were heated to 75 °C under stirring at 300 rpm and an Ar atmosphere. Later, 2 mL of TEOS were added dropwise for an hour and a half. The resulting suspensions were cooled to room temperature and the resulting powders were separated by magnetic decantation, washed with a 1:1 EtOH:H_2O solution and dried at 75°C for 2 h. The obtained samples were called as ($Y_{0.9}Er_{0.1}VO_4$/Fe_3O_4)@SiO_2-2 and ($Y_{0.9}Tm_{0.1}VO_4$/Fe_3O_4)@SiO_2. In addition, to study the effect of silica coating thickness, the erbium sample was prepared again in the same way but reducing the volume of TEOS added to 1 mL. The obtained sample was called as ($Y_{0.9}Er_{0.1}VO_4$/Fe_3O_4)@SiO_2-1.

The same process was also used to obtain the [($Y_{0.9}Ln_{0.1}VO_4$@SiO_2)/Fe_3O_4@SiO_2] nanocomposites with Ln = Er or Tm, which were prepared using only $Y_{0.9}Er_{0.1}VO_4$@SiO_2 and $Y_{0.9}Tm_{0.1}VO_4$@SiO_2 samples with addition of 1 mL of TEOS.

2.4. Characterization

XRD patterns of the synthesized samples were recorded on a PANalytical XPERT-PRO diffractometer, using Cu Kα radiation with a step of 0.04° and a counting time of 1 s per step. The instrumental broadening of the diffraction peaks was calibrated by using the LaB_6 standard NIST SRM 660b. The average crystallite size for each synthetized pure sample was calculated from diffraction profiles using Scherrer's formula for spherical particles [33]: $D = \frac{0.89\lambda}{\beta\cos(\theta)}$ where λ is the wavelength of Cu Kα radiation used in X-ray diffraction, β is the full width at half maximum (FWHM) and θ the diffraction angle.

Fourier transform infrared (FTIR) spectra were recorded employing a Spectrum Two FT-IR spectrophotometer in the 400–4000 cm^{-1} range with a resolution of 4 cm^{-1}. The powders were pressed against a diamond for measurements.

The morphological characterization of synthetized powders was carried out by transmission electron microscopy (TEM), using a JEOL JEM 2100 instrument, operating at 200 kV with a 0.25 nm resolution. For TEM observations, samples were dispersed in n-butanol and drops of the corresponding suspension were deposited on carbon-coated copper grids.

M *vs.* H curves were collected on a SQUID (Superconducting Quantum Interference Device) Quantum Design MPMS XL magnetometer, operating at 5, 150 and 300 K with a maximum applied field of up to 5000 Oe. ZFC/FC curves were measured using the same instrument and applying a constant field of 500 and 900 Oe. For the ZFC measures, the samples were cooled from 300 to 5 K, without applying an external field. The magnetic field was then applied as temperature rose and the magnetic susceptibility variation was recorded. In the FC measurements, the magnetic field was applied during the cooling step.

For recording of the photoluminescence (PL) emission spectra in the 300–1000 nm range, samples were excited using a pulsed Ti:shapphire laser at 360 nm and five measurements were made in one second for each sample. The powders were suspended in distilled water using 1 cm width quartz cuvettes. The emission spectrum of the powder samples was recorded in the NIR region (900–1600 nm) and excited by an 808 nm laser diode. The illumination density was controlled by setting at 5937 mW with an acquisition time of 5 s for the coated and uncoated $Y_{0.9}Ln_{0.1}VO_4$ samples and 23 s for the bifunctional samples. In addition, a short-pass filter (Thorlabs FES0850) was placed in front of the laser fiber to minimize specular and diffuse reflection effects. The emitted and scattered light was spectrally filtered with two consecutive long-pass filters (Thorlabs FEL0850) to block the 808 nm backscattered signal. Finally, the equipment consists of a combination of a short-wave infrared (SWIR) lens and a second tubular lens to focus the filtered light into a near-infrared camera (ZephIRTM 1.7) to produce a monochromatic image. The spectral range was obtained after recording each monochromatic image and continuously adjusting the angle of the BTF rotation stage. At the end of this process, the system built an HSI cube.

3. Results and discussion

3.1. X-ray diffraction study of $Y_{0.9}Ln_{0.1}VO_4$ and Fe_3O_4 samples

The evolution of XRD patterns with heating of the precursor powders of $Y_{0.9}(Er/Tm)_{0.1}VO_4$ samples is shown in Fig. 1.

After treatment of the precursor powders at 200°C (see Fig. 1a and c), diffraction maxima of different impurities can be observed in the corresponding XRD profiles of these samples. These impurities correspond to the following oxides: V_2O_5 of orthorhombic symmetry, space group Pmm and Z = 2 [JCPDS card file n° 01–089–2482],

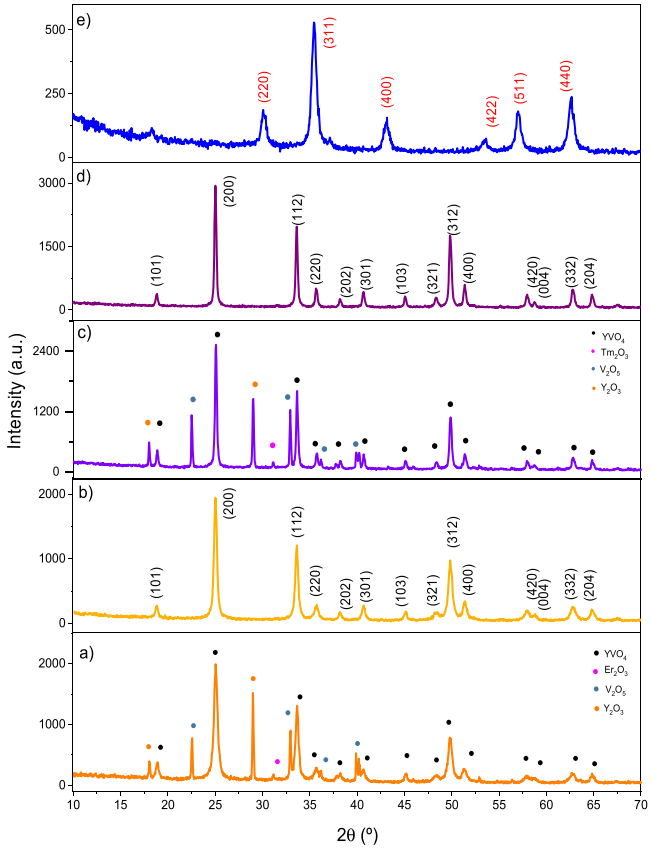

Fig. 1. XRD patterns of the powders: (a) $Y_{0.9}Er_{0.1}VO_4$ (after treatment at 220 ºC), (b) $Y_{0.9}Er_{0.1}VO_4$ (after treatment at 500 ºC), (c) $Y_{0.9}Tm_{0.1}VO_4$ (after treatment at 220 ºC), (d) $Y_{0.9}Tm_{0.1}VO_4$ (after treatment at 550 ºC) and (e) Fe_3O_4.

Table 1
Crystallographic parameters of $Y_{0.9}Ln_{0.1}VO_4$ and Fe_3O_4 samples.

Sample	a = b (Å)	c (Å)	V (Å^3)	D (nm)
$Y_{0.9}Er_{0.1}VO_4$	7.101(4)	6.277(4)	316.3(6)	24
$Y_{0.9}Tm_{0.1}VO_4$	7.098(0)	6.273(5)	316.3(5)	34
YVO_4*	7.1183	6.2893	318.68	–
Sample	a = b = c (Å)		V (Å^3)	D(nm)
Fe_3O_4	8.370(6)		586.5(2)	20
Fe_3O_4**	8.3969		592.05	-

* YVO_4 [JCPDS file card nº 01–082–1968]
** Fe_3O_4 [JCPDS card file nº 01–079–0419]

Y_2O_3 of cubic symmetry, space group $Fm\bar{3}m$ and Z = 2 [JCPDS card file n° 00–043–0661], as well as Er_2O_3 and Tm_2O_3, both of cubic symmetry, space group $Ia\bar{3}$ and Z = 16 [JCPDS card file n° 01–077–0464 and 00–010–0350, respectively]. The further heating to 500 °C leads to obtaining pure phases (see Fig. 1b and d) whose reflections can be indexed to a tetragonal symmetry of space group $I4_1/amd$ with Z = 4 [JCPDS file card n° 01–082–1968], compatible with a zircon structure-type. Secondary reflections were not observed within the sensitivity of the experimental system used, indicating that Tm^{3+} and Er^{3+} ions remained incorporated into the structure occupying the D_{2d} positions of the Y^{3+} ions and they were not segregated as oxides. Therefore, the purity of these two prepared samples was ensured. On the other hand, although both the obtaining method and the treatment used were equivalent, somewhat more intense diffraction maxima can be observed in the XRD profile of thulium sample, which may indicate a greater crystallinity of the obtained powder [31].

Lattice parameters and cell volume of pure samples were calculated from XRD patterns of Fig. 1 and using *Checkcell* software (see Table 1). Lattice parameters and cell volume determined for the $Y_{0.9}Ln_{0.1}VO_4$ samples are slightly lower than those of the YVO_4 oxide, in good agreement with the Shannon ionic radii values of erbium and terbium ions located in bisphenoids: Y^{3+} (1.019 Å), Er^{3+} (1.004 Å) and Tm^{3+} (0.994 Å) [34]. The effect of lanthanide contraction explains a lower value of the cell parameters in the thulium sample [35].

XRD patterns of Fe_3O_4 sample are also shown in Fig. 1. As indicated in the profile, all diffraction maxima can be indexed to a cubic symmetry of space group $Fd\bar{3}m$ with Z = 8 [JCPDS card file n° 01–079–0419]. Secondary reflections were not observed within the sensitivity of the experimental system used, which indicated the purity of the sample. The lattice parameter is between that of pure magnetite sample (8.3965 Å) and that of pure (γ-Fe_2O_3) maghemite (8.3515 Å) [1]. As P. Arévalo et al. and M. Fernández-Ramos et al. have already reported, the maghemite phase (γ-Fe_2O_3) may also be present since its diffraction maxima matched with those of magnetite, so it is also possible that our sample contains a small percentage of the maghemite phase [1,9].

In all cases, the mean crystal size of these samples (see Table 1) was calculated using Scherrer's formula and considering the diffraction maxima corresponding to the (200), (112), (312) planes for orthovanadate samples, and that of the (220), (311), (440) planes for iron oxide sample. Values between 20 and 34 nm confirmed the nanometric nature of the powders obtained.

Fig. 2 shows a perspective of the zircon structure-type and of the inverse spinel structure-type present in the obtained orthovanadates and Fe_3O_4 samples. In the first view Fig. 2a, the Y^{3+}/Tm^{3+}/Er^{3+} ions are found in the center of bisdysphenoids sharing edges along the *a*-axis, while the V^{5+} ions appear in a tetrahedral oxygen coordination along the *c*-axis, sharing opposite edges with the bisdysphenoid chains [4,36]. In the second view Fig. 2b, octahedral chains of [FeO_6] octahedra sharing edges along the diagonals of the cube faces are also linked by [FeO_4] tetrahedra sharing vertices. In this way, Fe^{2+} ions occupy half of the octahedral sites and Fe^{3+} ions are distributed between the remaining octahedral sites and the tetrahedral sites [1,16].

3.2. X-ray diffraction study of silica covered samples

XRD patterns of some silica coated samples are shown in Fig. 3.

In all cases, diffraction maxima of each of the pure phases are observed together with a very broad and weak diffraction maximum between 2θ = 15–25°, which indicates that the presence of amorphous silica [37] does not alter the structure of the samples.

3.3. FTIR spectroscopy studies

FTIR spectra of Fe_3O_4 and $Y_{0.9}Ln_{0.1}VO_4$ samples with Ln = Er or Tm, before and after of TEOS reaction are shown in Fig. 4.

A band with very strong intensity at 556 cm^{-1} appears in the FTIR spectra of synthesized uncoated and silica coated Fe_3O_4 samples. This band can be assigned to the asymmetric stretching mode of Fe-O bonds of the iron ions located in the tetrahedral positions of the inverse spinel structure-type. Another band at about 430 cm^{-1} is attributed to the stretching vibrations of Fe-O bonds of the Fe^{3+} and Fe^{2+} ions located in the octahedral positions of this structure. Its lower wavenumber is related to longer Fe-O bond lengths in octahedral positions than in tetrahedral ones [3,9,16].

New bands appear in the FTIR spectra of Fe_3O_4@SiO_2 sample. The band at 1064 cm^{-1} with a shoulder at 1215 cm^{-1} can be assigned to

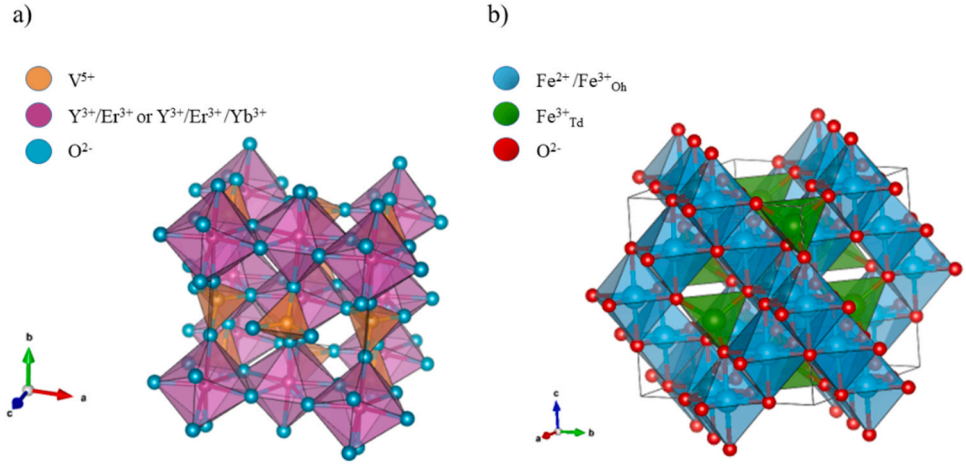

Fig. 2. Structures of (a) orthovanadates and (b) Fe_3O_4 samples.

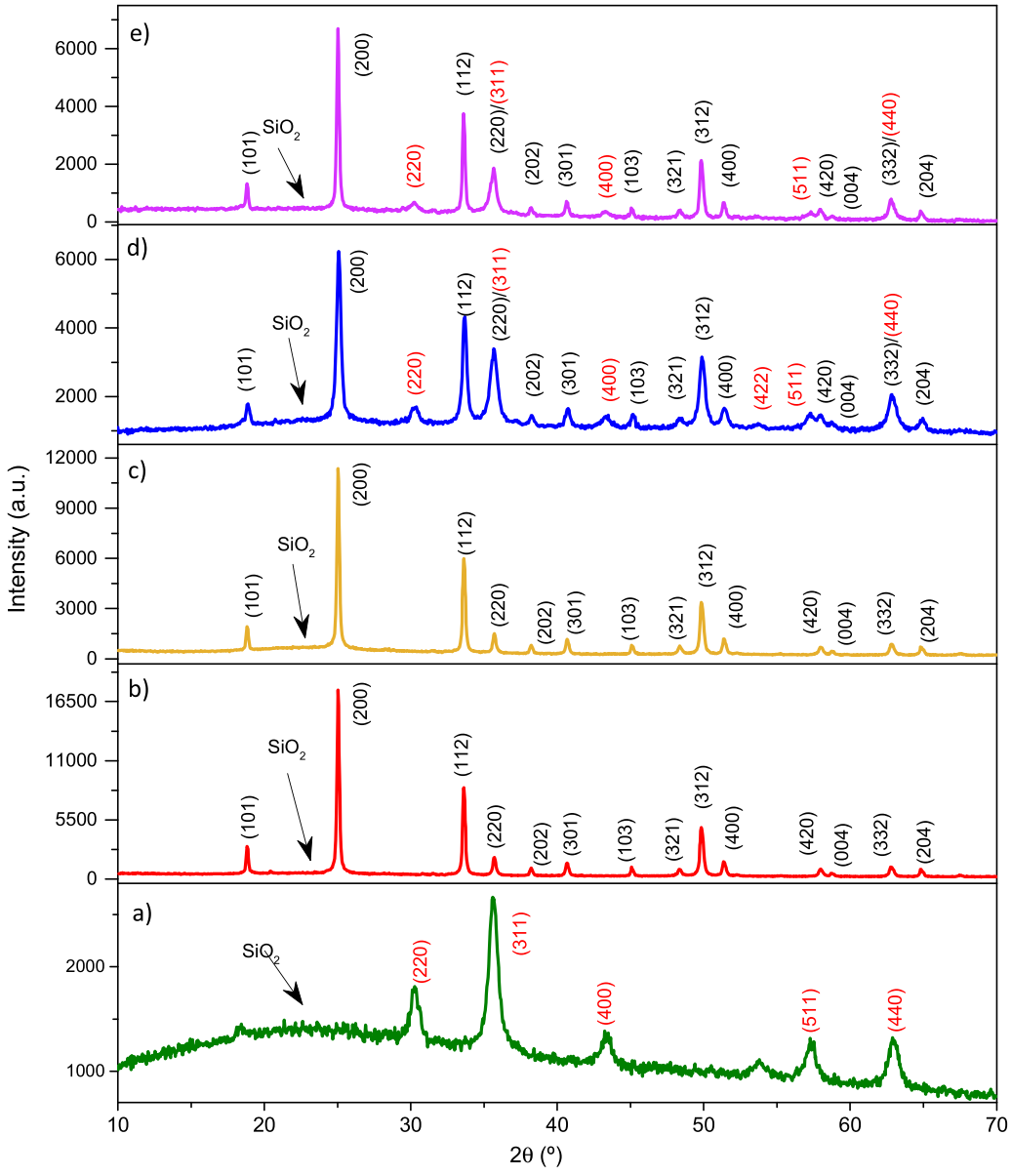

Fig. 3. XRD patterns of resulting samples after of TEOS reaction: (a) Fe_3O_4@SiO_2, (b) $Y_{0.9}Er_{0.1}VO_4$@SiO_2, (c) $Y_{0.9}Tm_{0.1}VO_4$@SiO_2, (d) ($Y_{0.9}Er_{0.1}VO_4$/Fe_3O_4)@SiO_2-2 and (e) ($Y_{0.9}Tm_{0.1}VO_4$ /Fe_3O_4)@SiO_2 samples.

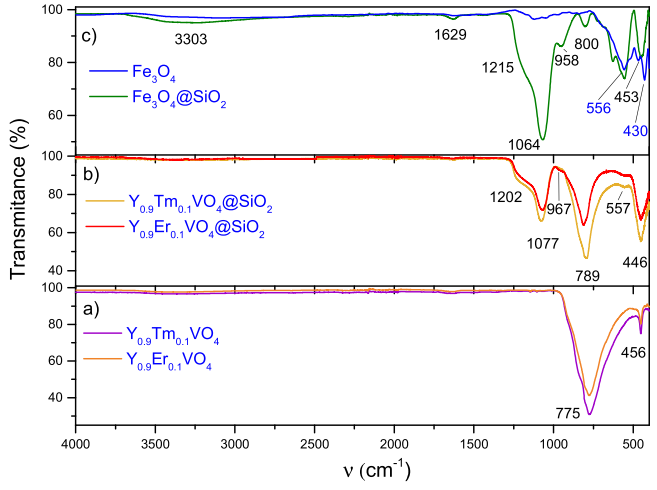

Fig. 4. FTIR spectra of the synthetized samples.

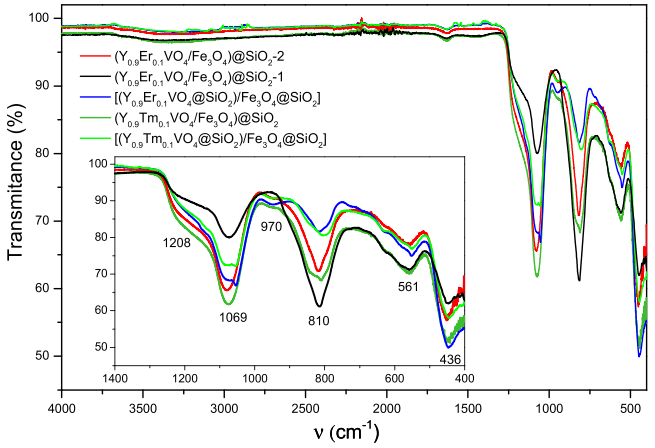

Fig. 5. FTIR of silica-covered erbium and thulium samples.

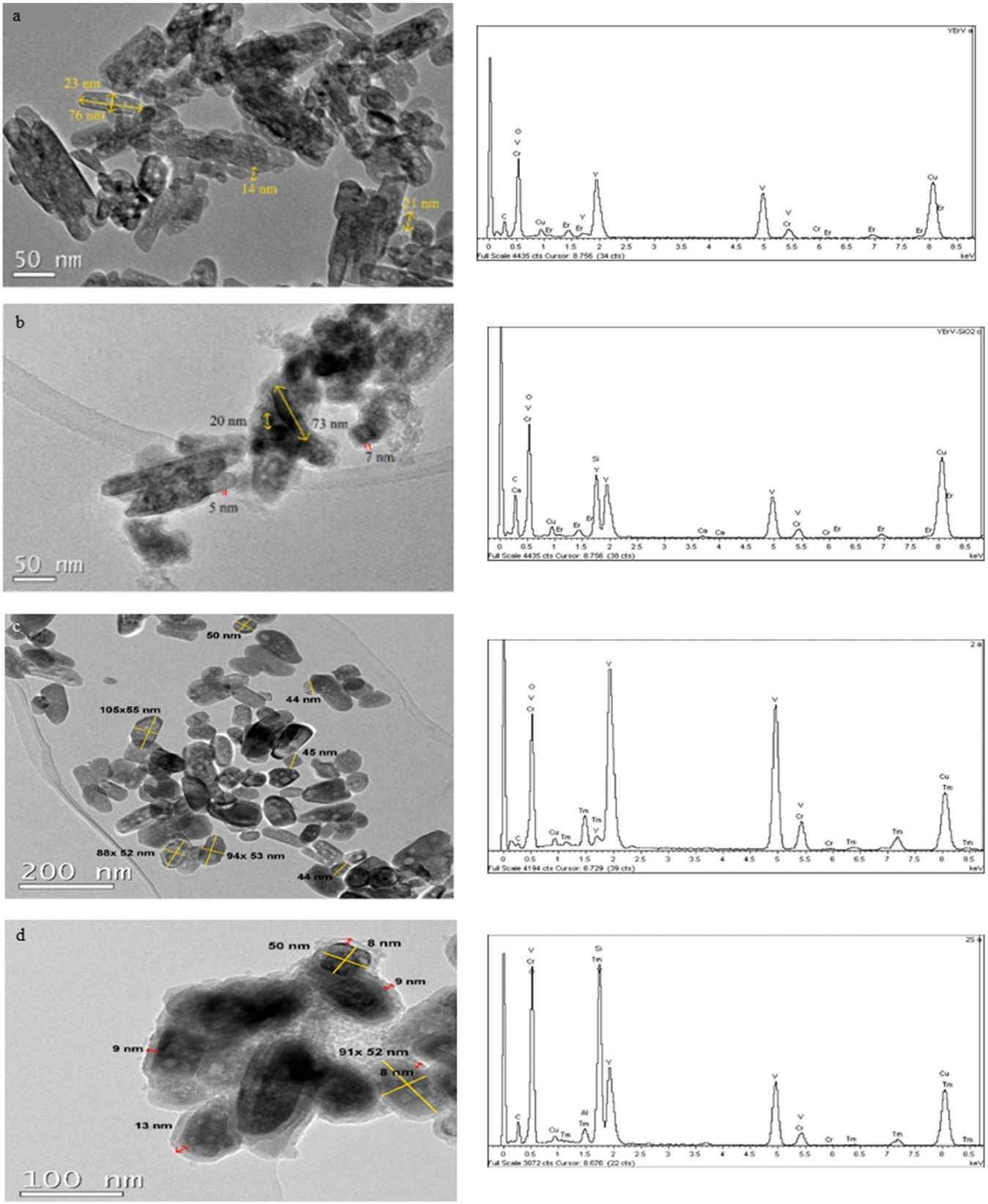

Fig. 6. TEM images and EDS analysis of uncoated and silica coated samples: (a) $Y_{0.9}Er_{0.1}VO_4$, (b) $Y_{0.9}Er_{0.1}VO_4@SiO_2$, (c) $Y_{0.9}Tm_{0.1}VO_4$ and (d) $Y_{0.9}Tm_{0.1}VO_4@SiO_2$.

the asymmetric stretching vibration of the Si-O-Si and O-Si-O stretching vibration modes, respectively [1,4,8,9]. The weak band observed at 958 cm^{-1} can be assigned to the stretching mode of the silanol group (Si-OH) [4,9,38,39]. The band at 453 cm^{-1} can be assigned to the in-plane bending vibration of the Si-O bonds, and the band at 565 cm^{-1} corresponds mainly to contributions of the ν(Fe-O) mode of the iron ions located in the tetrahedral positions and to a minor contribution of the Si-O-Fe bonds [1,9]. The band around

800 cm^{-1} can be assigned to the stretching vibration of the O-Si-O bonds. Finally, the two very weak bands at 3303 and 1629 cm^{-1} correspond to the stretching and bending modes of the O-H bonds around the SiO_2 surface, respectively [40].

In the FTIR of non- covered orthovanadate samples two bands are observed. The first one at 456 cm^{-1} can be assigned to the antisymmetric stretching vibration of the Y/Er^{3+}-O and Y/Tm^{3+}-O bonds, while the second broader and more intense band at 775 cm^{-1} is attributed to the antisymmetric stretching vibration of the V-O bonds in the VO_4^{3-} groups [7,9,20,30,36]. A new strong band appears in the FTIR spectra of $Y_{0.9}Ln_{0.1}VO_4@SiO_2$ at 1077 cm^{-1} with a small shoulder around 1202 cm^{-1} assignable to asymmetric stretching vibration modes of Si-O-Si and O-Si-O bonds, respectively [13,19,41]. The band detected at 446 cm^{-1} can be related to that observed in the uncoated sample spectrum at 456 cm^{-1}, although it now appears broadened due to the overlap with the bending vibration of the Si-O bonds [13,41]. Finally, two very weak bands are observed at 967 cm^{-1} and 557 cm^{-1} in the FTIR of $Y_{0.9}Ln_{0.1}VO_4@SiO_2$ samples that can be assigned to the stretching vibration of the silanol group (Si-OH) and to the stretching mode in four-membered siloxane $(SiO)_4$ rings, respectively [4,42].

FTIR of silica covered $(Y_{0.9}Ln_{0.1}VO_4/Fe_3O_4)@SiO_2$ and $[(Y_{0.9}Ln_{0.1}VO_4@SiO_2)/Fe_3O_4@SiO_2]$ samples with Ln = Er and Tm are shown in Fig. 5. In all these spectra, bands are again observed at 1208, 1069, 970, 810 cm^{-1} that are assignable to asymmetric stretching vibration modes of O-Si-O and Si-O-Si bonds [1,4,8,9], to the stretching vibration of silanol groups [4,38] and to the asymmetric stretching vibration of the V-O bonds in VO_4^{3-} groups, respectively [9,30,36]. The strong band at 436 cm^{-1} can also be assigned to the asymmetric stretching vibration of the Y/Er^{3+}-O and Y/Tm^{3+}-O bonds, but coupled with both, the in-plane antisymmetric bending vibration of the Si-O bonds and the asymmetric stretching vibrations of the Fe-O bonds located in the octahedral sites [24]. Finally, the band at 561 cm^{-1} is assigned to the asymmetric stretching vibrations of Fe-O bonds located in the tetrahedral sites of the inverse spinel [1,3,16].

Comparing FTIR spectra of erbium and thulium samples, it is observed that they appear overlapped. This fact indicates that the small difference in size of these atoms hardly deforms the crystal structure. However, the FTIR spectrum of $(Y_{0.9}Er_{0.1}VO_4/Fe_3O_4)@SiO_2$-2 sample shows a higher intensity band at 436 cm^{-1} than in FTIR spectrum of $(Y_{0.9}Er_{0.1}VO_4/Fe_3O_4)@SiO_2$-1 sample. This band can be assigned to the asymmetric stretching vibration of the Y/Er^{3+}-O and Y/Tm^{3+}-O bonds, but coupled with both, the in-plane antisymmetric bending vibration of the Si-O bonds and the asymmetric stretching vibrations of the Fe-O bonds located in the octahedral sites. This feature indicates a higher proportion of orthovanadate with respect to the silica incorporated in these nanocomposites. This result can be interpreted because a smaller amount of TEOS was used (1 mL *vs.* 2 mL of TEOS). This fact is also observed in the band centered at 1069 cm^{-1}, which is less intense in the Er-doped bifunctional sample using only 1 mL of TEOS.

3.4. Transmission electron microscopy

TEM images of $Y_{0.9}Ln_{0.1}VO_4$ and $Y_{0.9}Ln_{0.1}VO_4$ $@SiO_2$ samples wit Ln = Er or Tm are shown in Fig. 6. Particle size distribution graphs were made by measuring at least 80 particles using the ImageJ software (National Institutes of Health, USA). Particles of two different morphologies are observed in the erbium samples: rounded of 14–21 nm and elongated of a size between 25 × 15–60 nm. Particles with similar morphologies, but larger in size, are also found in the thulium samples: rounded 42–50 nm and elongated with dimensions between 108 and 88 × 55 nm. These values differ from those calculated with the Scherrer equation of 24 and 34 nm from XRD patterns and this feature occurs because for their calculation it was assumed that all particles were spherical [8,29] and this is not the case. We have found similar morphology in samples of the same type synthesized at basic pH [30].

As can be observed in Fig. 6, coating tests with TEOS were successful. A thin silica shell between 5 and 13 nm thicknesses can be found in the environment of individualized particles. Atomic percentages determined from EDS microanalysis confirm the compositions of uncoated samples and reveal a percentage between 35% and 42.3% of silica incorporated in the two silica coated samples. The additional signals observed in EDS spectra of carbon (C) and copper (Cu) are due to the carbon-coated copper grids used for the measurements.

TEM images of Fe_3O_4 and $Fe_3O_4@SiO_2$ samples are shown in Fig. 7. Aggregated spherical particles are found, but individual particles with a mean diameter of 14 ± 3 nm can also be distinguished. This value is of the same order as that calculated from the XRD data (20 nm). The observed particle agglomeration may be due to long-distance magnetic dipole-dipole interaction that originates between these particles [20]. In TEM image of $Fe_3O_4@SiO_2$ sample, nanoparticles coated with a silica shell of 8 nm thicknesses can be seen. Iron and silicon atomic percentages determined from EDS microanalysis confirm the Fe_3O_4 composition and reveal a percentage of 42.3% of silica incorporated in the silica coated sample.

TEM images of $(Y_{0.9}Ln_{0.1}VO_4/Fe_3O_4)@SiO_2$ samples with Ln = Er and Tm are shown in Figs. 8 and 9. Nanoparticles of Fe_3O_4 sample (circled in red) and others that are orthovanadate powders (circled in yellow) are observed. All these particles are agglomerated and enclosed in a full and homogeneous silica shell between 7 and 12 nm thickness. TEM images of $[(Y_{0.9}Ln_{0.1}VO_4$ $@SiO_2/Fe_3O_4)@SiO_2]$ samples show nanoparticles (see Fig. 9) of Fe_3O_4 (circled in red) in silica bags of 6–8 nm thickness (circled in yellow) together with nanoparticles of orthovanadate powders (circled in green), and this whole group included in a second silica bag of 15–19 nm thickness. EDS microanalysis are in good agreement with the nominal compositions and reveal a higher percentage of silica in the $(Y_{0.9}Er_{0.1}VO_4/Fe_3O_4)@SiO_2$-2 sample (59.4%), which was prepared with 2 mL of TEOS, with respect to $(Y_{0.9}Er_{0.1}VO_4/Fe_3O_4)@SiO_2$-1 sample (32.70%) prepared with 1 mL of TEOS. However, in the $(Y_{0.9}Tm_{0.1}VO_4/Fe_3O_4)@SiO_2$ sample that was only prepared with 2 mL of TEOS, a percentage of 50.52% was found, very similar to that of the erbium sample prepared in the same way. In the $[(Y_{0.9}Er_{0.1}VO_4@SiO_2/Fe_3O_4)@SiO_2]$ and $[(Y_{0.9}Er_{0.1}VO_4@SiO_2/Fe_3O_4)@SiO_2]$ samples these percentages are somewhat higher, 67.5% and 66.1%, respectively, as expected considering their preparation.

3.5. Magnetic behavior studies

Fig. 10 shows the variation of magnetization, M, with the applied magnetic field, H, at three different temperatures for Fe_3O_4 and Fe_3O_4 $@SiO_2$ samples. Table 2 summarizes the magnetic parameters that are determined from these plots.

Fig. 9 shows a sigmoid curve at 300 K and almost at 150 K that confirms the typical superparamagnetic behavior of Fe_3O_4 and $Fe_3O_4@SiO_2$ samples. This behavior can also be observed considering the very low coercive field values (see Table 2) determined at 300 and 150 K (8.7 Oe and 50.4 Oe for Fe_3O_4 sample and 23.8 Oe and 49.7 Oe for $Fe_3O_4@SiO_2$ sample, respectively) [9,10]. By contrast, at 5 K a typical ferrimagnetic behavior is found because of the wider hysteresis loop associated with a high coercive field value (265.2 Oe for Fe_3O_4 sample and 264.3 for $Fe_3O_4@SiO_2$ sample) [10]. A decrease in temperature causes the blocking of the magnetic moments of the particles, which leads to an increase in the coercivity H_c [43]. This means that at 5 K the magnetic spins of the particles are more constrained in their movement to orient in the applied field direction. At higher temperatures, the magnetic spins that form the nanoparticles monodomain can rotate freely due to the high thermal

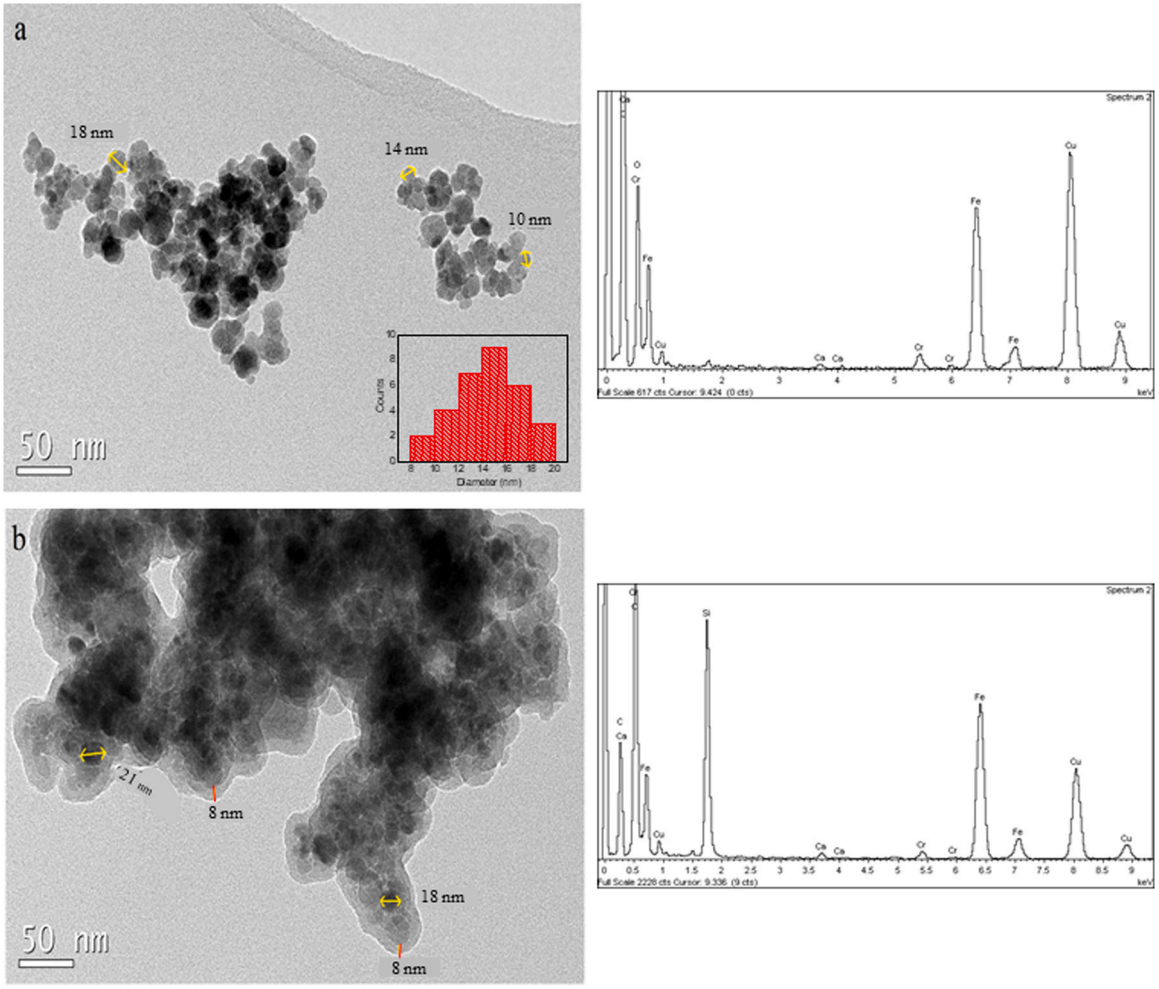

Fig. 7. TEM images and EDS analysis of uncoated and silica coated samples: (a) Fe_3O_4 with particle size distribution and (b) Fe_3O_4@SiO_2.

energy. This feature occurs above the so-called blocking temperature (T_B). However, below this temperature the magnetic anisotropy increases with respect to the thermal energy and thus it bocks the spins [37]. At 5 K, the thermal energy is not enough to overcome the anisotropy energy barrier in the Fe_3O_4 and Fe_3O_4@SiO_2 samples, leading them to ferrimagnetic behavior [39].

The M_r/M_s ratio (see Table 2) also confirms this effect, since at lower temperatures the remanent magnetization (M_r) is higher than at 150 K and 300 K. Thus, it is confirmed that uncoated and silica coated Fe_3O_4 samples, containing particles of 20 nm in average size, are superparamagnetic at 300 K due to the almost null value of the coercive field at room temperature [25] and it remains almost null at 150 K. These features indicate that they can be useful in the 300 – 150 K range in applications that involve directing them with external magnetic fields.

On the other hand, as can be observed in Table 2, the Fe_3O_4 sample shows a decrease in saturation magnetization, which becomes more noticeable at 300 K with respect to the theoretical value of bulk magnetite (92 emu/g) [9,16]. This value will vary slightly because the magnetic properties are directly related to the shape and size of the particles [16]. This decrease is observed in nanometric-sized magnetic materials due to surface effects produced by the particle size reduction, where the magnetic moments are tilted on the surface and lose directionality [24]. The spin canted layer of magnetic nanoparticles is higher with smaller particle size, where M_s varies according to Eq. 2 [44].

$$M_s = M_s(\text{bulk})\left(1 - \frac{6t}{D}\right) \tag{2}$$

In this equation, M_s (bulk) is the magnetization of the material in its bulk form, t is the spin canting layer thickness and D is the particle diameter.

The values determined in this work for Fe_3O_4 sample (see Table 2) are like those reported by Guardia et al., (Ms ≈ 80–85 emu/g at 5 K) in nanoparticles with a size between 4 and 20 nm [16,27]. Moreover, when analyzing the diffraction profile of iron oxide sample, it may contain a small percentage of the maghemite phase with lower magnetization (82 emu/g) than magnetite [9], which could also explain the low values determined for Ms. As expected, a lower saturation magnetization value is determined for Fe_3O_4@SiO_2 sample. It is since the 8 nm of amorphous silica shell that surrounds

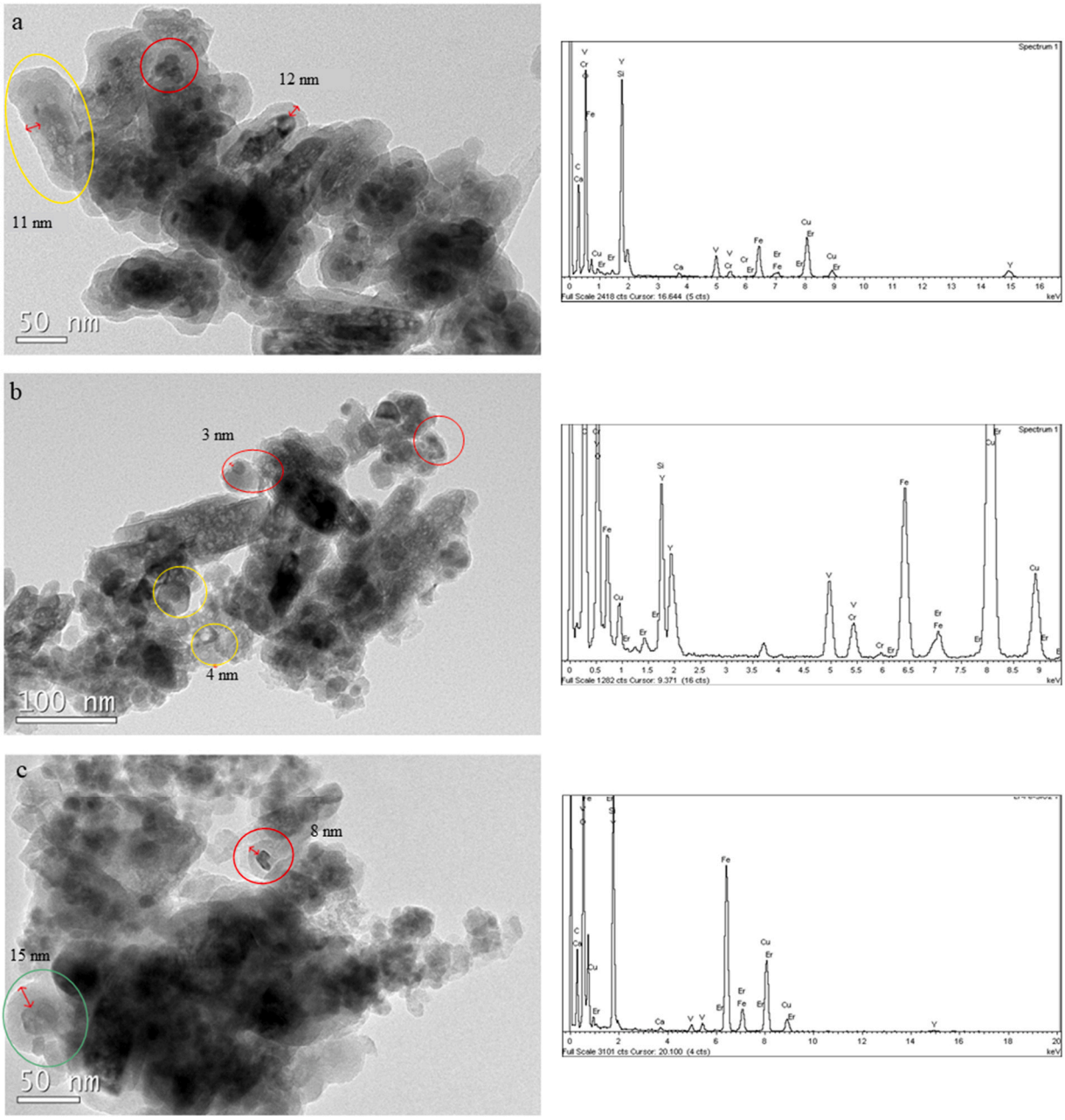

Fig. 8. TEM images and EDS analysis of silica coated samples: (a) $(Y_{0.9}Er_{0.1}VO_4/Fe_3O_4)@SiO_2$-2, (b) $(Y_{0.9}Er_{0.1}VO_4/Fe_3O_4)@SiO_2$-1 and (c) $[(Y_{0.9}Er_{0.1}VO_4@SiO_2)/Fe_3O_4@SiO_2]$.

the Fe_3O_4 magnetic nanoparticles (Fig. 7) causes a spin disorder or spin tilts on the surfaces that hinder the magnetic exchange interactions between Fe_3O_4 magnetic sublattices [38,43].

It is known that the presence of disordered spins on the nanoparticles surface of Fe_3O_4 and $Fe_3O_4@SiO_2$ samples could modify the energy that each particle must overcome to reach the maximum saturation magnetization [43]. For this reason, Zero Field Cooled (ZFC) and Field Cooled (FC) measurements were carried out by applying a constant field higher than that corresponding to the magnetic anisotropy value of bulk magnetite (≈ 400 Oe) [45]. ZFC and FC magnetic susceptibility curves are shown in Fig. 11. In all of them it can be observed that the ZFC curve increases with temperature increment and reaches the maximum value at the blocking temperature (T_B). At that temperature, the energy barrier of the magnetic anisotropy of the nanoparticle is overcome by the thermal activation energy [43]. For an applied field of 500 Oe, a T_B value of 52 K is determined for the Fe_3O_4 sample and of 56 K for $Fe_3O_4@SiO_2$ sample. In both cases, above T_B the magnetization decreases sharply as the temperature increases [11]. The FC and ZFC curves coincide and overlap at high temperatures. At that point, the system is unlocked, and the rotation of magnetic moments is thermally allowed for a given applied field. However, when the temperature decreases, the ZFC and FC curves separate due to larger particles blocking, which occurs at a temperature value that is called the irreversibility

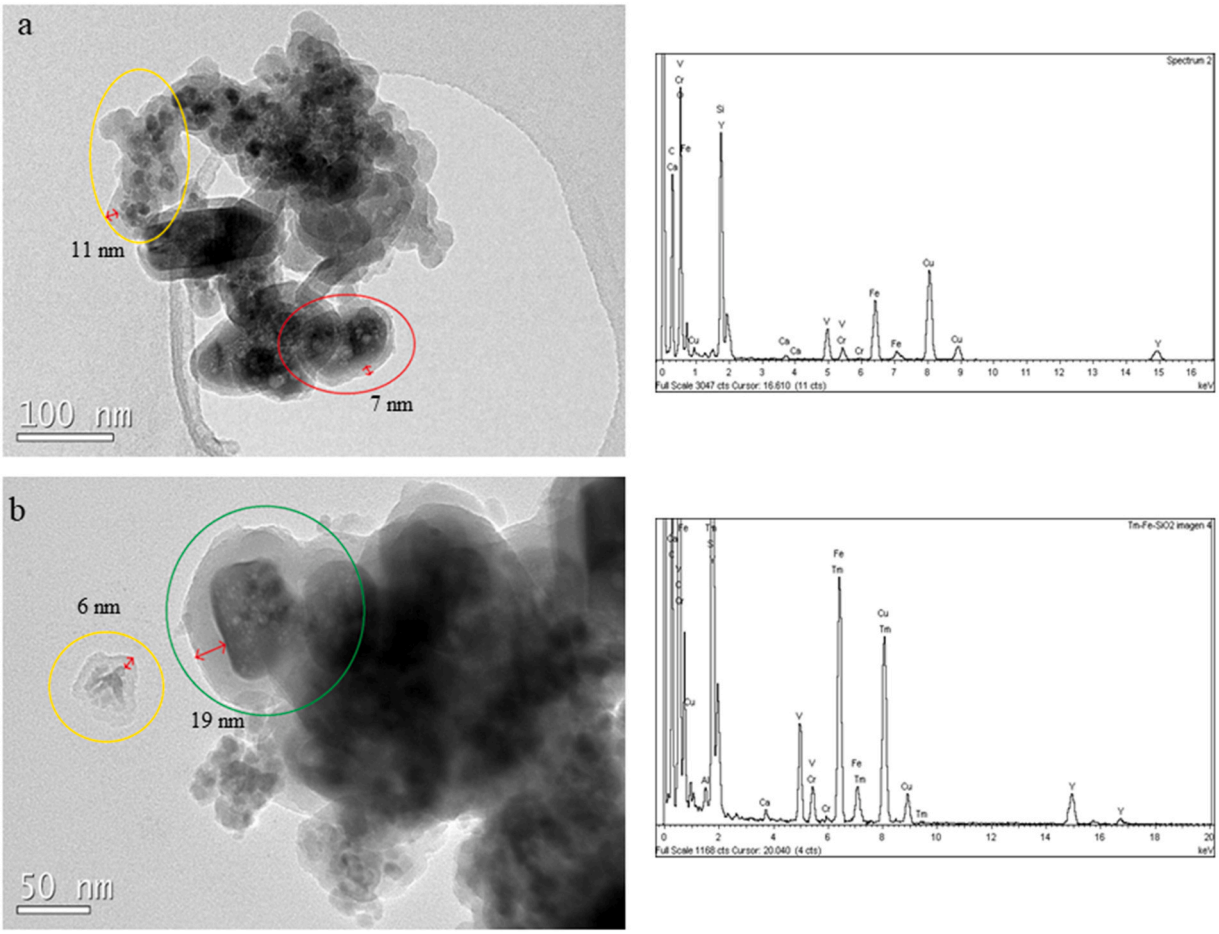

Fig. 9. TEM images and EDS analysis of silica coated samples: (a) $(Y_{0.9}Tm_{0.1}VO_4/Fe_3O_4)@SiO_2$ and (b) $[(Y_{0.9}Tm_{0.1}VO_4@SiO_2/Fe_3O_4)@SiO_2]$.

temperature (T_{irr}). This value is146 K for Fe_3O_4 sample and 183 K for silica covered sample. It is observed that both T_B and T_{irr} increase in the $Fe_3O_4@SiO_2$ sample due to the 8 nm silica shell, Fig. 7, which surrounds the magnetic particles, increasing their size and therefore, causing these particles to block at higher temperatures [43,46].

It can also be observed in Fig. 11 that the values of T_B and T_{irr} decrease as the value of the applied field increases from 500 to 900 Oe. The values at 900 Oe are T_B = 212 K and T_{irr} = 261 K. This result can be explained considering that when a more intense magnetic field is applied, the magnetic moments orientation of each particle is favored, forcing the change towards lower values of the unlocked ↔ locked state transition [37]. This feature is in accordance with Eq. 3 [47], where the TB value increases with the magnetic field increment.

$$T_B \approx \frac{K\,V(1 - H/H_k)^2}{25\,k_B} \tag{3}$$

In this equation, *K* is the anisotropy constant, V the mean volume of the particles and $H_k = \mu_0 \cdot M_s/2\,K$. For the superparamagnetism phenomenon to take place, the working temperature must be higher than the blocking temperature. It explains why in the M *vs*. H curves at 300 K a narrow cycle characteristic of a superparamagnetic material is observed, while when measuring at 5 K, a temperature lower than the T_B value observed in the ZFC/FC curves, the hysteresis cycle is wide and characteristic of a ferrimagnetic material. In addition, as can be seen in Fig. 10, the magnetic susceptibility is lower in the $Fe_3O_4@SiO_2$ sample because of the effect caused by the silica coat, which makes the particles less sensitive to a magnetic field, as it is observed in the hysteresis loops.

Hysteresis loops at room temperature of silica coated orthovanadate and iron oxide mixture samples are shown in Fig. 12. Magnetic parameters determined from these plots are also shown in Table 2.

As expected, the Ms value for these samples is between 27.3 and 20.2 emu/g, which is lower than that of the $Fe_3O_4@SiO_2$ sample, 31.5 emu/g. This reduction was previously described by our research group for silica coated bifunctional samples doped with Nd and Tb lanthanides [1]. This effect is due to the incorporation of non-magnetic particles in the samples. However, it should be noted that these values could be high enough for these samples to be directed in response to the presence of an external magnetic field [3]. In the $(Y_{0.9}Er_{0.1}VO_4/Fe_3O_4)@SiO_2$-1 and $(Y_{0.9}Er_{0.1}VO_4/Fe_3O_4)@SiO_2$-2 samples, it is observed that the Ms, Mr and Hc values decrease with greater thickness of the coating shell and at the same time the magnetic response of the material decreases. The magnetic response of the remaining samples is very similar, although they have slightly more silica. Finally, it should also be noted that the Hc and M_r values are lower than those of the Fe_3O_4 and $Fe_3O_4@SiO_4$ samples (see Table 2). This means that bifunctional samples show a higher SPM

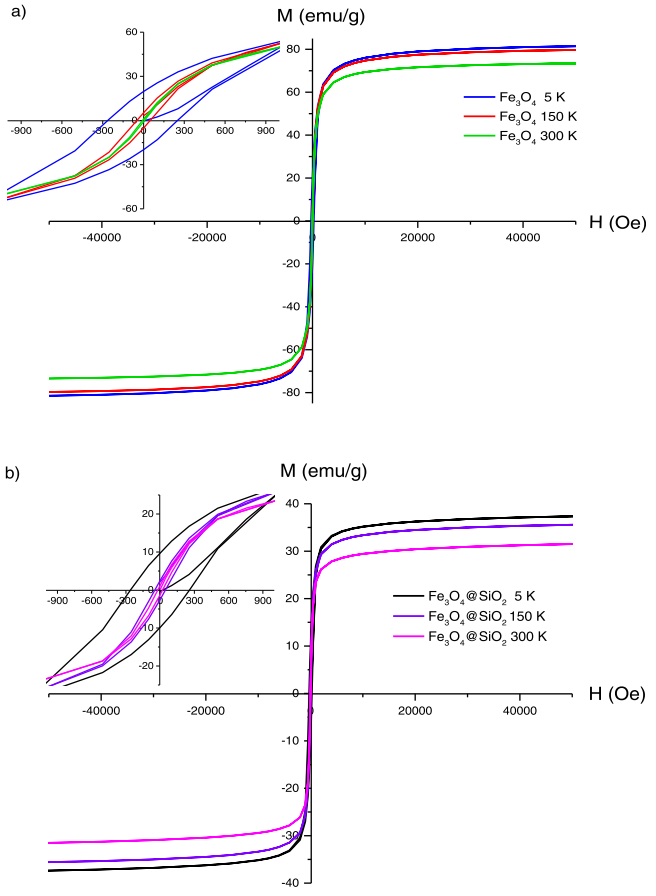

Fig. 10. Hysteresis loops of: (a) uncovered and (b) silica covered Fe_3O_4 samples (enlarged images of these hysteresis loops are also included).

behavior at room temperature, as we previously reported for silica coated bifunctional samples doped with Nd and Tb [1].

3.6. Emission luminescent studies

The PL emission spectra of $Y_{0.9}Er_{0.1}VO_4$, $Y_{0.9}Er_{0.1}VO_4@SiO_2$ and $(Y_{0.9}Er_{0.1}VO_4/Fe_3O_4)@SiO_2$-2 samples after photoexcitation at 360 nm radiation are shown in Fig. 13.

A first band appears at 354 nm that can be assigned to charge transfer between V^{5+}-O^{2-} ions [7,8,36]. The VO_4^{3-} groups acting as sensitizers absorb UV light photons and, once excited, transfer their energy to the Er^{3+} ions located in the D_{2d} sites [13,37]. As a result, a new band appears at 450 nm [36]. This energy transfer causes electrons to populate the $^4F_{7/2}$ level of the erbium ion, leading to non-radiative transits from this level to the $^2H_{11/2}$ and $^4S_{3/2}$ levels (see Fig. 13b). The presence of bands in the green region of the spectrum (at 532 and 564 nm) is the result of the $^2H_{11/2} \rightarrow {}^4I_{15/2}$ and $4S_{3/2} \rightarrow {}^4I_{15/2}$ electronic transitions [34,41].

Silica coatings are intended to minimize nanoparticle surface defects and thus lead to an increase in emission intensity in the PL spectra. However, the opposite was observed in the coated samples with a decrease in emission intensity. This decrease can be explained considering that the amorphous silica-coating contains a large amount of silanol groups (Si-OH) on its surface. These groups have a

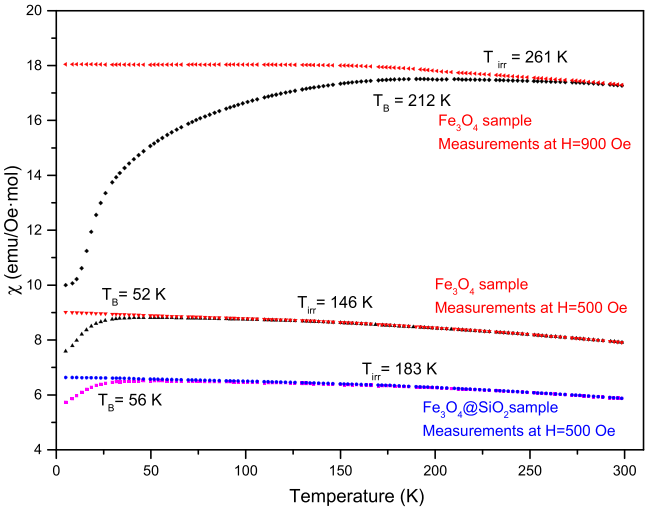

Fig. 11. Zero field cooled (ZFC) and field cooled (FC) curves.

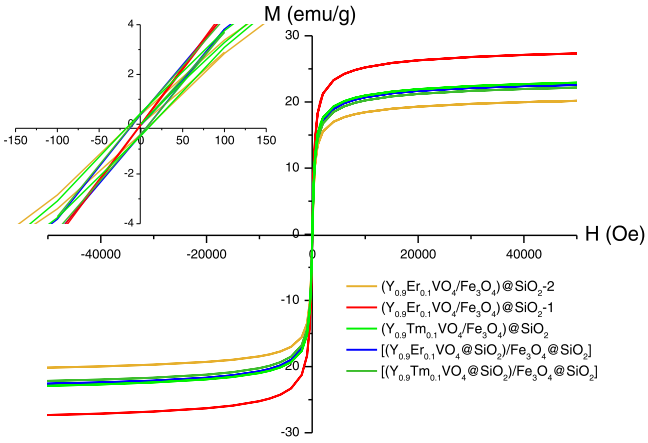

Fig. 12. Hysteresis loops of silica coated mixture samples.

Table 2
Magnetic parameters determined from hysteresis loops of all synthetized samples.

Sample	T (K)	M_s (emu/g)	M_r (emu/g)	H_c (Oe)	M_r/M_s	Thickness (nm)
Fe_3O_4	5	81.4	19.7	265.2	0.24	–
	150	79.7	5.2	50.4	0.07	
	300	73.4	0.9	8.7	0.01	
$Fe_3O_4@SiO_2$	5	37.4	9.7	264.3	0.26	8
	150	35.6	2.3	49.7	0.06	
	300	31.5	1.0	23.8	0.03	
$(Y_{0.9}Er_{0.1}VO_4/Fe_3O_4)@SiO_2$-1	300	27.3	1.6	3.6	0.06	4
$(Y_{0.9}Er_{0.1}VO_4/Fe_3O_4)@SiO_2$-2	300	20.2	1.5	17.2	0.07	12
$(Y_{0.9}Tm_{0.1}VO_4/Fe_3O_4)@SiO_2$	300	22.9	1.6	17.5	0.07	13
$[(Y_{0.9}Er_{0.1}VO_4@SiO_2)/Fe_3O_4@SiO_2]$	300	22.6	1.8	13.2	0.08	14
$[(Y_{0.9}Tm_{0.1}VO_4@SiO_2)/Fe_3O_4@SiO_2]$	300	22.2	1.7	14.0	0.08	10

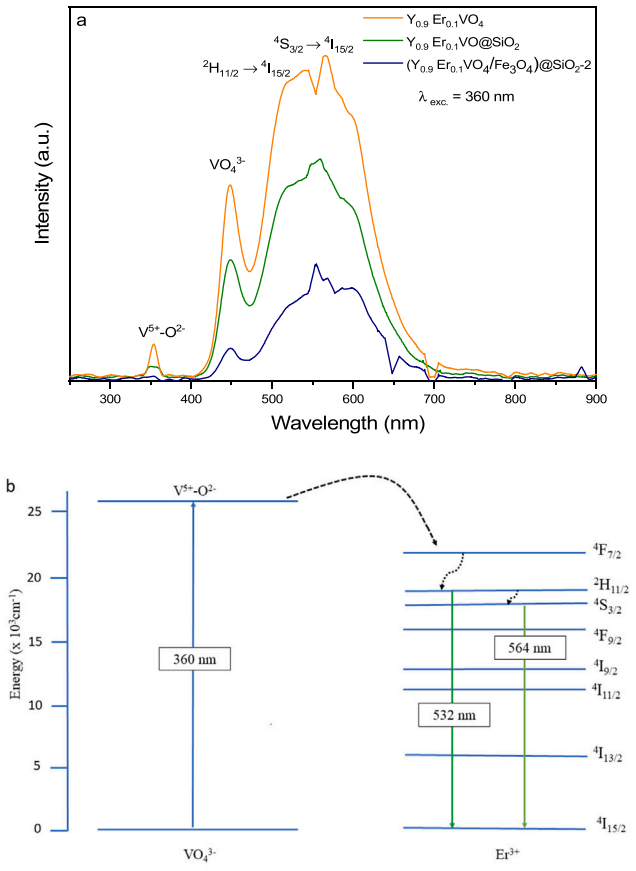

Fig. 13. (a) PL emission spectra of erbium samples with UV excitation and (b) down-conversion process shown in the Er^{3+} ion energy level diagram.

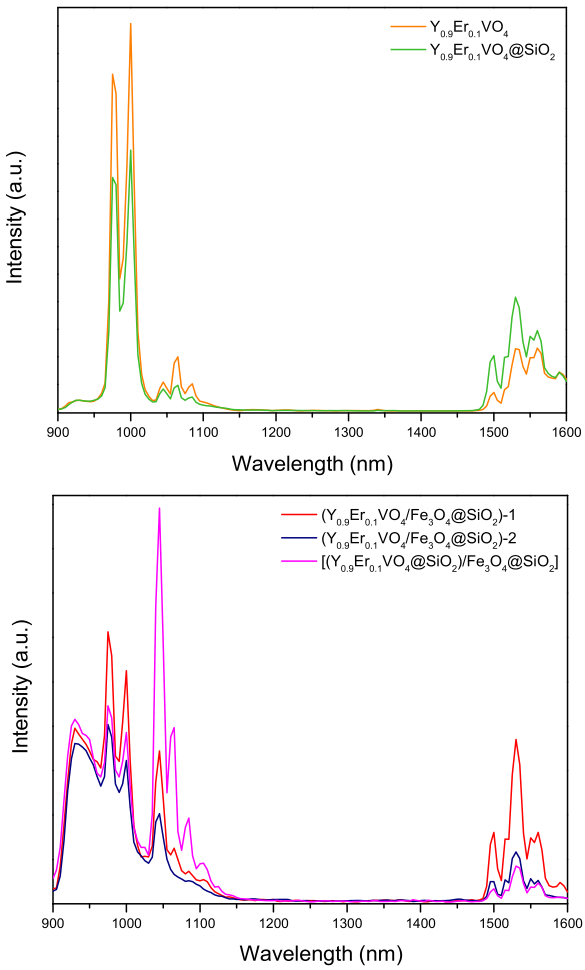

Fig. 14. PL emission spectra with photoexcitation at 808 nm of erbium samples.

high phonon energy that favors the multiphonon relaxation process and inhibits the radiative processes of Er^{3+} ions. This phenomenon is frequently observed on functionalized surfaces with hydroxyl groups that participate in luminescence quenching of rare earth ions due to their high vibrational frequencies [48,49]. This reduction in luminescence can also be explained by the thickness (5–12 nm) of the coating shell [8]. In addition, in the PL spectra of $(Y_{0.9}Er_{0.1}VO_4/Fe_3O_4)$ @SiO_2-2 sample a greater decrease in emission intensity is observed. This feature can be explained by considering the high thickness of the silica shell together with the quenching effect of the iron oxide that occurred during sample excitation [3].

Finally, all synthesized samples were investigated for their possible application as fluorescent probes. Thus, it was found that after being excited with ultraviolet light, the emission of erbium or thulium ions was masked. However, this emission did not occur when the samples were excited with IR radiation, since this radiation increases the detection sensitivity [4,8,50]. Therefore and for comparison purposes, with an excitation at 808 nm the emission PL spectra of $Y_{0.9}Ln_{0.1}VO_4$, $Y_{0.9}Ln_{0.1}VO_4@SiO_2$, $(Y_{0.9}Ln_{0.1}VO_4/Fe_3O_4)@SiO_2$-2, $(Y_{0.9}Er_{0.1}VO_4/Fe_3O_4)@SiO_2$-1 and $[(Y_{0.9}Ln_{0.1}VO_4@SiO_2)/Fe_3O_4@SiO_2]$ samples with Ln = Er and Tm dispersed in deionized water are shown in Figs. 14 and 15. In the PL spectra of erbium samples, two strong bands can be observed: the first one at 985 nm can be assigned to the $^4I_{11/2} \rightarrow {}^4I_{15/2}$ electronic transition occurred in this ion, while the second band between 1500 and 1570 nm is attributed to the $^4I_{13/2} \rightarrow {}^4I_{15/2}$ electronic transition [51]. However, the emission band centered at 1550 nm showed a lower intensity than that at 985 nm with low quantum yield in the $^4I_{13/2} \rightarrow {}^4I_{15/2}$ electronic transition due to the strong energy transfer from the Er^{3+} ions to the OH^- groups of the water where they were dispersed. Hydroxyl groups are an important quencher for Er^{3+}down-conversion emission, leading to a decrease in emission intensity after hydrophilic coating with silica, as can be observed in the coated samples of Figs. 14 and 15 [49,52].

The emission spectra of thulium samples in Fig. 15a show a band at 1464 nm that can be assigned to the $^3H_4 \rightarrow {}^3F_4$ [16] electronic transition and another band around 1065 nm, but with the strongest intensity of the spectrum, and assigned to the $^1G_4 \rightarrow {}^3H_4$ electronic transitions of Tm^{3+} ions. In addition, two weak bands appear at 1340 and 1220 nm corresponding to the $^3F_3 \rightarrow {}^3F_4$ and $^1G_4 \rightarrow {}^3H_4$ electronic transitions of Tm^{3+} ions, respectively [53,54].

A greater decrease in emission intensity is observed in all samples with iron oxide, which may be due to both, the high thickness of the silica shell and the iron oxide acting as a quencher during the excitation process of samples. However, a higher emission intensity can be found in the $[(Y_{0.9}Ln_{0.1}VO_4@SiO_2)/Fe_3O_4@SiO_2]$ sample than those of other iron oxide samples, indicating that the silica precoating of the $Y_{0.9}Ln_{0.1}VO_4$ sample prevents the iron oxide particles from being close to the fluorescent particles, thus minimizing the quenching effect.

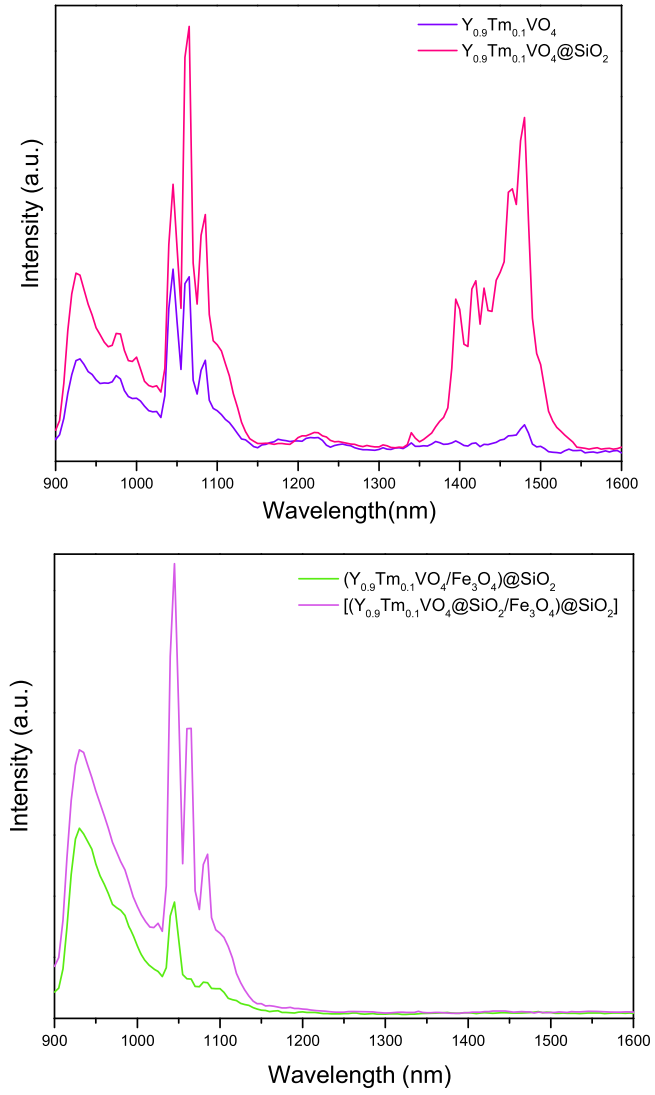

Fig. 15. PL emission spectra with photoexcitation at 808 nm of thulium samples.

4. Conclusions

For the first time, we have synthesized bifunctional samples formed by luminescent $Y_{0.9}Ln_{0.1}VO_4$ samples with Ln = Er or Tm and magnetic Fe_3O_4 sample. These nanopowders were successfully linked as mixtures through a silica coating. The bifunctional samples retain the superparamagnetic behavior of Fe_3O_4 nanoparticles at room temperature as it is observed in the M *vs.* H measurements. The final synthesized magnetic-fluorescent bifunctional samples also maintain the luminescence emission characteristic of rare earth ions, but their intensity is reduced. An increase in the silica shell thickness and the presence of iron appear to act as a quencher of the luminescence of the erbium and thulium ions. However, those samples that have the magnetic and luminescent cores separated by a silica wall have their emission intensity less reduced. Therefore, we have found that the bifunctional $[(Y_{0.9}Ln_{0.1}VO_4@SiO_2)/Fe_3O_4@SiO_2]$ samples seem the most suitable to be used as display systems with the possibility of directing them by means of external magnetic fields.

CRediT authorship contribution statement

María Rapp: Research, Software images, Original draft preparation. Sending the paper. **Yaiza Lozano:** Research, Software images, Original draft preparation. **Miguel Fernández-Ramos:** Software images, Original draft preparation. **Josefa Isasi:** Original draft, Supervision, Validation. **Mauricio Alcolea Palafox:** Supervision, Validation.

Declaration of Competing Interest

The authors declare that they have no known competing financial interests or personal relationships that could have appeared to influence the work reported in this paper.

Acknowledgements

This work was financially supported by the Spanish Ministry of Science and Innovation, through project PID2019-106211RB-I00. We thank the ICTS National Center for Electron Microscopy of the UCM for access and the NanoBig research group led by Daniel Jaque, and especially to José Lifante for the help provided in the measurements carried out there.

Data availability

The raw/processed data required to reproduce these findings cannot be shared at this time due to technical or time limitations.

References

[1] M. Fernández-Ramos, J. Isasi, M. Alcolea, T. Muñoz-Ortiz, E. Ortiz-Rivero, New magnetic-fluorescent bifuntional ($Y_{0.9}Ln_{0.1}VO_4/Fe_3O_4$)@$SiO_2$ and [($Y_{0.9}Ln_{0.1}VO_4$@ SiO_2)/Fe_3O_4@SiO_2] materials, Ceram. Int. (2022), https://doi.org/10.1016/j.ceramint.2022.04.191

[2] J. Shi, L. Tong, X. Ren, Q. Li, H. Yang, Multifunctional Fe_3O_4@ C/YVO_4: Dy^{3+} nanopowers: preparation, luminescence, and magnetic properties, Ceram. Int. 39 (6) (2013) 6391–6397, https://doi.org/10.1016/j.ceramint.2013.01.065

[3] G.S. Ningombam, D. Chattopadhyay, K. Sarkar, S.N. Kalkura, N.R. Singh, Luminescent water dispersible core-shell–(Y/Eu/Li)VO_4@ APTES@Folate and (Y/Eu/Li)VO_4@ Fe_3O_4@ PEG nanocomposites: biocompatibility and induction heating within the threshold alternating magnetic field, Colloids Surf. A Physicochem. Eng. Asp. 625 (2021) 126826, https://doi.org/10.1016/j.colsurfa.2021.126826

[4] M. Rapp, J. Isasi, M.A. Palafox, T. Muñoz-Ortiz, E. Ortiz-Rivero, Synthesis, structural and morphological characterization and photoluminescence study of $Y_{0.9}Er_{0.1-x}Yb_xVO_4$ materials, J. Alloy. Compd. 163930 (2022), https://doi.org/10.1016/j.jallcom.2022.163930

[5] C.T.B. Thao, B.T. Huy, M. Sharipov, J.-I. Kim, V.-D. Dao, J.-Y. Moon, Y.-I. Lee, Yb^{3+}, Er^{3+}, Eu^{3+}-codoped YVO_4 material for bioimaging with dual mode excitation, Mater. Sci. Eng. C 75 (2017) 990–997, https://doi.org/10.1016/j.msec.2017.02.169

[6] H. Xia, R. Tong, Y. Song, F. Xiong, J. Li, S. Wang, H. Fu, J. Wen, D. Li, Y. Zeng, Synthesis and bio-applications of targeted magnetic-fluorescent composite nanoparticles, J. Nanopart. Res. 19 (4) (2017) 1–10, https://doi.org/10.1007/s11051-017-3833-7

[7] L.R. Singh, Eu^{3+} as a marker for formation of core-shell system: YVO_4:SiO_2, OpenNano 2 (2017) 57–63, https://doi.org/10.1016/j.onano.2017.01.002

[8] L. Alcaraz, J. Isasi, Synthesis and study of $Y_{0.9}Ln_{0.1}VO_4$ nanophosphors and $Y_{0.9}Ln_{0.1}VO_4$@ SiO_2 luminescent nanocomposites with Ln= Eu, Dy, Er, Ceram. Int. 43 (6) (2017) 5311–5318, https://doi.org/10.1016/j.ceramint.2017.01.069

[9] P. Arévalo-Cid, J. Isasi, F. Martín-Hernández, Comparative study of core-shell nanostructures based on amino-functionalized Fe_3O_4@SiO_2 and $CoFe_2O_4$@SiO_2 nanocomposites, J. Alloy. Compd. 766 (2018) 609–618, https://doi.org/10.1016/j.jallcom.2018.06.246

[10] A. Mohammadi, M. Barikani, Synthesis and characterization of superparamagnetic Fe_3O_4 nanoparticles coated with thiodiglycol, Mater. Charact. 90 (2014) 88–93, https://doi.org/10.1016/j.matchar.2014.01.021

[11] M.S. Beg, J. Mohapatra, L. Pradhan, D. Patkar, D. Bahadur, Porous Fe_3O_4-SiO_2 core-shell nanorods as high-performance MRI contrast agent and drug delivery vehicle, J. Magn. Magn. Mater. 428 (2017) 340–347, https://doi.org/10.1016/j.jmmm.2016.12.079

[12] W.W. You, D.T. Tu, W. Zheng, X.Y. Shang, X.R. Song, S.Y. Zhou, Y. Liu, R.F. Li, X.Y. Chen, Large-Scale synthesis of uniform lanthanide-doped $NaREF_4$ upconversion/downshifting nanoprobes for bioapplications, Nanoscale 10 (2018) 11477–11484, https://doi.org/10.1039/C8NR03252A

[13] L. Zhang, X.D. Li, W. Wang, X. Zhao, X. Yan, C.G. Wang, H.Q. Bao, Y. Lu, X.G. Kong, F.M. Liu, X.M. Liu, G.Y. Lu, Construction of self-sensitized $LiErF_4$: 0.5%Tm^{3+}@$LiYF_4$ upconversion nanoprobe for trace water sensing, Nano Res. 13 (2020) 2803–2811, https://doi.org/10.1007/s12274-020-2932-4

[14] B.S. Cao, Y.N. Bao, Y. Liu, J.Y. Shang, Z.Y. Zhang, Y.Y. He, Z.Q. Feng, B. Dong, Wide-range and highly-sensitive optical thermometers based on the temperature-dependent energy transfer from Er to Nd in Er/Yb/Nd codoped $NaYF_4$

upconversion nanocrystals, Chem. Eng. J. 385 (2020) 123906, https://doi.org/10.1016/j.cej.2019.123906
[15] K. Lu, Y. Yi, L. Xu, X. Sun, L. Liu, H. Li, Temperature-independent lifetime and thermometer operated in a biological window of upconverting NaErF4 nanocrystals, Nanomaterials 10 (1) (2020) 24, https://doi.org/10.3390/nano10010024
[16] W. Wu, Z. Wu, T. Yu, C. Jiang, W.-S. Kim, Recent progress on magnetic iron oxide nanoparticles: synthesis, surface functional strategies and biomedical applications, Sci. Technol. Adv. Mater. (2015), https://doi.org/10.1088/1468-6996/16/2/023501
[17] D. Zharkov, A. Shmelev, A. Leontyev, V. Nikiforov, V. Lobkov, M. Alkahtani, P. Hemmer, V. Samartsev, Light converting Yb^{3+}/Er^{3+} doped YVO_4 nanoparticles for biological applications, Laser Phys. Lett. 17 (7) (2020) 075901, https://doi.org/10.1088/1612-202X/ab9115
[18] S.A. Khrushchalina, P.A. Ryabochkina, M.N. Zharkov, V.M. Kyashkin, N.Y. Tabachkova, I.A. Yurlov, Broadband emission from Er-contained yttrium orthophosphate and orthovanadate nanopowders excited by near infrared radiation, J. Lumin. 205 (2019) 560–567, https://doi.org/10.1016/j.jlumin.2018.09.030
[19] S. Pattnaik, M. Mondal, L. Mukhopadhyay, S. Basak, V.K. Rai, R. Giri, V. Singh, Frequency upconversion based thermally stable molybdate phosphors in a temperature sensing probe, New J. Chem. (2022), https://doi.org/10.1039/D2NJ01105K
[20] X. Zhou, J. Shen, Y. Wang, Z. Feng, R. Wang, L. Li, S. Jiang, X. Luo, An efficient dual-mode solar spectral modification for c-Si solar cells in Tm^{3+}/Yb^{3+} codoped tellurite glasses, J. Am. Ceram. Soc. 99 (7) (2016) 2300–2305, https://doi.org/10.1111/jace.14133
[21] P. Huang, D. Chen, Y. Wang, Host-sensitized multicolor tunable luminescence of lanthanide ion doped one-dimensional YVO_4 nano-crystals, J. Alloy. Compd. 509 (7) (2011) 3375–3381, https://doi.org/10.1016/j.jallcom.2010.12.069
[22] D. Chen, Y. Yu, P. Huang, H. Lin, Z. Shan, L. Zeng, A. Yang, Y. Wang, Color-tunable luminescence for Bi^{3+}/Ln^{3+}:YVO_4 (Ln= Eu, Sm, Dy, Ho) nanophosphors excitable by near-ultraviolet light, Phys. Chem. Chem. Phys. 12 (28) (2010) 7775–7778, https://doi.org/10.1039/C003678A
[23] M.N. Luwang, R.S. Ningthoujam, S.K. Srivastava, R.K. Vatsa, Preparation of white light emitting YVO_4:Ln^{3+} and silica-coated YVO_4:Ln^{3+} (Ln^{3+}= Eu^{3+}, Dy^{3+}, Tm^{3+}) nanoparticles by CTAB/n-butanol/hexane/water microemulsion route: energy transfer and site symmetry studies, J. Mater. Chem. 21 (14) (2011) 5326–5337, https://doi.org/10.1039/C0JM03470C
[24] C. Ferrer, J. Isasi, P. Arévalo, M. Fernández-Ramos, M. Rapp, M. Alcolea, J. Marco, F. Martín-Hernández, Structural and magnetic studies of $NiFe_2O_4$ and $NiFe_2O_4$@ SiO_2-Silane agent samples useful for the removal of Cu^{2+} ions, J. Alloy. Compd. 899 (2022) 163403, https://doi.org/10.1016/j.jallcom.2021.163403
[25] X. Zhang, L. Hao, H. Wang, X. Zhu, Z. Zhang, X. Hu, W. Jiang, Preparation and characterization of superparamagnetic Fe_3O_4/CNTs nanocomposites dual-drug carrier, J. Wuhan Univ. Technol. Mater. Sci. Ed. 32 (1) (2017) 42–46, https://doi.org/10.1007/s11595-017-1555-4
[26] P. Decuzzi, B. Godin, T. Tanaka, S.-Y. Lee, C. Chiappini, X. Liu, M. Ferrari, Size and shape effects in the biodistribution of intravascularly injected particles, J. Control. Release 141 (3) (2010) 320–327, https://doi.org/10.1016/j.jconrel.2009.10.014
[27] P. Guardia, A. Labarta, X. Batlle, Tuning the size, the shape, and the magnetic properties of iron oxide nanoparticles, J. Phys. Chem. C 115 (2) (2011) 390–396, https://doi.org/10.1021/jp1084982
[28] I. Gonzalo-Juan, B. Ferrari, M. Colomer, Influence of the urea content on the YSZ hydrothermal synthesis under dilute conditions and its role as dispersant agent in the post-reaction medium, J. Eur. Ceram. Soc. 29 (15) (2009) 3185–3195, https://doi.org/10.1016/j.jeurceramsoc.2009.04.041
[29] B. Srinivasan, E. Kolanthai, N. Eluppai Asthagiri Kumaraswamy, R.R. Jayapalan, D.S. Vavilapalli, L.H. Catalani, G.S. Ningombam, N.S. Khundrakpam, N.R. Singh, S.N. Kalkura, Thermally modified iron-inserted calcium phosphate for magnetic hyperthermia in an acceptable alternating magnetic field, J. Phys. Chem. B 123 (26) (2019) 5506–5513, https://doi.org/10.1021/acs.jpcb.9b03015
[30] L. Alcaraz, J. Isasi, C. Díaz-Guerra, Influence of the synthesis conditions of $Y_{0.9}Dy_{0.1}VO_4$ and silica-coated $Y_{0.9}Dy_{0.1}VO_4$ nanophosphors on the powder morphology and luminescence emission intensity, J. Nanopart. Res. 21 (4) (2019) 1–13, https://doi.org/10.1007/s11051-019-4514-5
[31] L. Alcaraz, J. Isasi, C. Díaz-Guerra, Effects of preparation method and pH variation on the structural characteristics and luminescence properties of $Y_{0.9}Er_{0.1}VO_4$ and $Y_{0.9}Er_{0.1}V_{0.9}Cr_{0.1}O_4$ nanopowders, J. Lumin. 165 (2015) 105–114, https://doi.org/10.1016/j.jlumin.2015.04.038
[32] J. Isasi, P. Arévalo, E. Martin, F. Martín-Hernández, Preparation and study of silica and APTES–silica-modified $NiFe_2O_4$ nanocomposites for removal of Cu^{2+} and Zn^{2+} ions from aqueous solutions, J. Sol Gel Sci. Technol. 91 (3) (2019) 596–610, https://doi.org/10.1007/s10971-019-05067-3
[33] P. Scherrer, Bestimmung der inneren Struktur und der Größe von Kolloidteilchen mittels Röntgenstrahlen, Kolloidchemie Ein Lehrbuch, Springer, 1912, pp. 387–409, https://doi.org/10.1007/978-3-662-33915-2_7
[34] S. Pattnaik, M. Mondal, L. Mukhopadhyay, S. Basak, V.K. Rai, R. Giri, V. Singh, Frequency upconversion based thermally stable molybdate phosphors in a temperature sensing probe, New J. Chem. (2022), https://doi.org/10.1016/j.jlumin.2019.02.008
[35] Rt Shannon, C. Prewitt, Revised values of effective ionic radii, Acta Crystallogr. Sect. B Struct. Crystallogr. Cryst. Chem. 26 (7) (1970) 1046–1048, https://doi.org/10.1107/S0567740870003576
[36] H. Li, N. Luo, D. Luo, L. Xiong, L. Yang, M. Zhao, Effect of calcination temperature on the microstructure and optical properties of monodispersed self-assembled yttrium orthovanadate microspheres, J. Lumin. 234 (2021) 117990, https://doi.org/10.1016/j.jlumin.2021.117990
[37] E.S.D.T. de Mendonça, A.C.B. de Faria, S.C.L. Dias, F.F. Aragon, J.C. Mantilla, J.A. Coaquira, J.A. Dias, Effects of silica coating on the magnetic properties of magnetite nanoparticles, Surf. Interfaces 14 (2019) 34–43, https://doi.org/10.1016/j.surfin.2018.11.005
[38] M. Mostafaei, S.N. Hosseini, M. Khatami, A. Javidanbardan, A.A. Sepahy, E. Asadi, Isolation of recombinant Hepatitis B surface antigen with antibody-conjugated superparamagnetic Fe_3O_4/SiO_2 core-shell nanoparticles, Protein Expr. Purif. 145 (2018) 1–6, https://doi.org/10.1016/j.pep.2017.12.004
[39] I.M. Obaidat, C. Nayek, K. Manna, Investigating the role of shell thickness and field cooling on saturation magnetization and its temperature dependence in Fe_3O_4/γ-Fe_2O_3 Core/Shell nanoparticles, Appl. Sci. 7 (12) (2017) 1269, https://doi.org/10.3390/app7121269
[40] A. Nikmah, A. Taufiq, A. Hidayat, Synthesis and characterization of Fe_3O_4/SiO_2 nanocomposites, IOP Conference Series: Earth and Environmental Science, IOP Publishing, 2019, p. 012046. ⟨https://doi.org/10.1088/1755–1315/276/1/012046⟩.
[41] V. Tamilmani, L. Mukhopadhyay, V.K. Rai, K.J. Sreeram, A.K. Mishra, Dual mode luminescence from lanthanum orthovanadate nanoparticles, J. Lumin. 217 (2020) 116761, https://doi.org/10.1016/j.jlumin.2019.116761
[42] L. Ruggiero, M.R. Fidanza, M. Iorio, L. Tortora, G. Caneva, M.A. Ricci, A. Sodo, Synthesis and characterization of TEOS coating added with innovative antifouling silica nanocontainers and TiO2 nanoparticles, Front. Mater. 7 (2020) 185, https://doi.org/10.3389/fmats.2020.00185
[43] K. Tadyszak, A. Kertmen, E. Coy, R. Andruszkiewicz, S. Milewski, I. Kardava, B. Scheibe, S. Jurga, K. Chybczyńska, Spectroscopic and magnetic studies of highly dispersible superparamagnetic silica coated magnetite nanoparticles, J. Magn. Magn. Mater. 433 (2017) 254–261, https://doi.org/10.1016/j.jmmm.2017.03.025
[44] C. Vázquez-Vázquez, M. López-Quintela, M. Buján-Núñez, J. Rivas, Finite size and surface effects on the magnetic properties of cobalt ferrite nanoparticles, J. Nanopart. Res. 13 (4) (2011) 1663–1676, https://doi.org/10.1007/s11051-010-9920-7
[45] M. Ahmadzadeh, C. Romero, J. McCloy, Magnetic analysis of commercial hematite, magnetite, and their mixtures, Aip Adv. 8 (5) (2018) 056807, https://doi.org/10.1063/1.5006474
[46] M. Polichetti, M. Modestino, A. Galluzzi, S. Pace, M. Iuliano, P. Ciambelli, M. Sarno, Influence of citric acid and oleic acid coating on the dc magnetic properties of Fe_3O_4 magnetic nanoparticles, Mater. Today Proc. 20 (2020) 21–24, https://doi.org/10.1016/j.matpr.2019.08.152
[47] I.J. Bruvera, P. Mendoza Zélis, M. Pilar Calatayud, G.F. Goya, F.H. Sánchez, Determination of the blocking temperature of magnetic nanoparticles: the good, the bad, and the ugly, J. Appl. Phys. 118 (18) (2015) 184304, https://doi.org/10.1063/1.4935484
[48] A.A. Ansari, M.M. Khan, Structural and spectroscopic studies of $LaPO_4$:Ce/Tb@ $LaPO_4$@ SiO_2 nanorods: synthesis and role of surface coating, Vib. Spectrosc. 94 (2018) 43–48, https://doi.org/10.1016/j.jmmm.2017.03.025
[49] Y. Wang, W. Qin, J. Zhang, C. Cao, S. Lü, X. Ren, Photoluminescence of colloidal YVO_4: Eu/SiO2 core/shell nanocrystals, Opt. Commun. 282 (6) (2009) 1148–1153, https://doi.org/10.1016/j.optcom.2008.12.007
[50] I. Kolesnikov, E. Golyeva, A. Kalinichev, M. Kurochkin, E. Lähderanta, M. Mikhailov, Nd^{3+} single doped YVO_4 nanoparticles for sub-tissue heating and thermal sensing in the second biological window, Sens. Actuators B Chem. 243 (2017) 338–345, https://doi.org/10.1016/j.snb.2016.12.005
[51] M.F. Ferreira, F.H.P. de Andrade, C.J. Granito, W.E. do Nascimento Melo, E.H. de Faria, K.J. Ciuffi, L.A. Rocha, E.J. Nassar, Non-hydrolytic sol–gel route: a powerful process to develop UV-Vis-IR luminescent YVO_4 phosphors, J. Fluoresc. 30 (2020) 827–837, https://doi.org/10.1007/s10895-020-02549-4
[52] A.A. Ansari, M.A. Majeed Khan, Structural and spectroscopic studies of $LaPO_4$:Ce/Tb@$LaPO_4$@SiO_2 nanorods: synthesis and role of surface coating, Vib. Spectrosc. 94 (2018) 43–48, https://doi.org/10.1016/j.vibspec.2017.12.001
[53] X. Zhou, J. Shen, Y. Wang, Z. Feng, R. Wang, L. Li, S. Jiang, X. Luo, An efficient dual-mode solar spectral modification for c-Si solar cells in Tm^{3+}/Yb^{3+} codoped tellurite glasses, J. Am. Ceram. Soc. 99 (2016) 2300–2305, https://doi.org/10.1111/jace.14133
[54] Y.Z. Wang, D.C. Yu, H.H. Lin, S. Ye, M.Y. Peng, Q.Y. Zhang, Broadband three-photon near-infrared quantum cutting in Tm^{3+} singly doped YVO_4, J. Appl. Phys. 114 (2013) 203510, https://doi.org/10.1063/1.4836897